Microstructure and Temperature Dependent Indentation Response of Additively Manufactured Precipitation-Strengthened $Al_{0.3}Ti_{0.2}Co_{0.7}CrFeNi_{1.7}$ High Entropy Alloy

MOHAN SAI KIRAN KUMAR YADAV NARTU [1,3] SHRISTY JHA,[2]
ADVIKA CHESETTI,[2] SUNDEEP MUKHERJEE,[2]
ISABELLA VAN ROOYEN,[1] and RAJARSHI BANERJEE[2,4]

1.—Nuclear Sciences Division, Pacific Northwest National Laboratory, Richland, WA 99354, USA.
2.—Department of Materials Science and Engineering, University of North Texas, Denton, TX 76207, USA. 3.—e-mail: m.nartu@pnnl.gov. 4.—e-mail: Raj.Banerjee@unt.edu

The temperature-dependent [from room temperature (RT) to 500°C] nanoindentation behavior of a precipitation-strengthened $Al_{0.3}Ti_{0.2}Co_{0.7}CrFeNi_{1.7}$ high-entropy alloy (HEA) processed via two different additive manufacturing (AM) techniques was investigated in the as-deposited and annealed conditions. The hierarchically heterogeneous microstructures were achieved via simple one-step annealing treatments, exploiting the residual stresses in the AM-processed HEA to partially recrystallize the microstructure, performed remarkably better than the nearly homogeneous microstructures in the as-deposited state. The one-step annealed conditions revealed < 6.6% reduction in hardness values at 500°C compared to RT, while the as-deposited conditions showed a > 18% reduction in the hardness. The one-step annealed conditions also exhibited significantly higher hardness than the as-deposited conditions owing to their $L1_2$-strengthened FCC microstructures. Furthermore, serrated yielding or the Portevin-Le Chatlier effect indicative of *microstructural instability* was observed during nanoindentation deformation (at 500°C) for the as-deposited conditions but not for the one-step annealed conditions. This, therefore, signifies the *robustness of the hierarchically heterogeneous microstructures at elevated temperatures* presenting a strong avenue for tuning the HEAs for future nuclear reactor applications.

INTRODUCTION

In recent times, there has been significant effort in developing new structural materials such as bulk metallic glasses (BMGs),[1–4] oxide dispersion strengthened (ODS) steels,[5–7] ceramics,[8–11] nanolayered composites,[12–16] and high-entropy alloys (HEAs)[17] for next-generation nuclear reactor applications. Structural materials need to sustain against creep and void swelling and exhibit reasonably high mechanical strength and fracture toughness under irradiation at high temperatures (> 300°C). According to Zinkle and Snead,[18] there are three main strategies for improving the radiation tolerance in materials: (1) designing radiation-resistant matrix phases, (2) immobilizing the vacancies and interstitials, and (3) enhancing the sink strength of the material. Among the new materials, HEAs are shown to address all three design strategies[17] and thus form an integral part of the advanced material development portfolio; they are the reason for further exploration of the current work.

High-entropy alloys (HEAs) with significantly higher configurational entropy than conventional alloys exhibit unusual lattice distortion and

Microstructure and Temperature Dependent Indentation Response of Additively
Manufactured Precipitation-Strengthened $Al_{0.3}Ti_{0.2}Co_{0.7}CrFeNi_{1.7}$ High Entropy Alloy

5047

sluggish diffusion, which could potentially immobilize the radiation-induced defects resulting in undesired swelling and segregation, which are detrimental to their mechanical and functional properties.[19–27] HEAs are worth considering, particularly for nuclear reactors, since the high levels of transmutation in conventional alloys may already produce compositionally complex alloys locally resembling HEAs.[17,28,29] While the first two strategies, (1) and (2) mentioned previously, can only augment the radiation resistance of the HEAs to a limited extent, the third strategy, (3) enhancing the sink strength of the material, can show multifold improvement in the radiation resistance.[30–32] One way to enhance the sink strength of the HEAs is to have multiple interfaces by either secondary phase precipitation or a multi-modal distribution of grain sizes, including nano-structured grains. HEAs offer significant potential for inducing such microstructural heterogeneities but the conventional processing route involving casting is tedious and time-consuming.[30,33–35] For instance, the microstructure of a transformation-induced plasticity (TRIP)-enabled HEA has been innovatively engineered by Agrawal et al.[30] for enhanced radiation resistance. The processing route involved a preliminary homogenization annealing of the cast HEA followed by a hot rolling to eliminate the cast defects. The rolled HEA was eventually descaled, heat treated at 500°C (desired phase field), and then finally warm-rolled to obtain a massively interfaced alloy.

In contrast, previous work by Nartu et al. (2022)[36] on $Al_{0.3}Ti_{0.2}Co_{0.7}CrFeNi_{1.7}$ HEA demonstrates a straightforward one-step annealing approach exploiting the residual stresses in additive manufacturing (AM) to successfully engineer the heterogeneous microstructures. This $L1_2$ precipitation strengthenable $Al_{0.3}Ti_{0.2}Co_{0.7}CrFeNi_{1.7}$ HEA is reported to exhibit a yield strength of ~1600 MPa with decent ductility at room temperature (RT) and is expected to have high-temperature stability up to ~1100°C.[33] This HEA was fabricated via two different AM techniques, directed energy deposition (DED) and selective laser melting (SLM), and the evolution of the heterogeneous microstructures in the as-deposited (AD) and subsequently annealed conditions and their tensile properties [at room temperature (RT)] has been reported by the authors.[36,37] However, the temperature-dependent mechanical behavior essential for nuclear applications was not yet investigated. This article provides a discussion on the microstructural differences as well as the temperature-dependent (from RT to 500°C) nanoindentation behavior of the heterogeneous microstructures obtained via one-step annealing post DED and SLM-processing of $Al_{0.3}Ti_{0.2}Co_{0.7}CrFeNi_{1.7}$ HEA. The differences in the nanoindentation behavior between the as-deposited and the one-step annealed conditions of the DED and SLM processed conditions are discussed.

MATERIALS AND METHODS

This study used the Optomec LENS-750 system equipped with an IPG YLS-1500 fiber laser system (with a maximum power output of 1500 W) for the directed energy deposition (DED) and Trumpf Tru-Print 1000 laser powder bed fusion system for selective laser melting (SLM). Pre-alloyed powders of $Al_{0.3}Ti_{0.2}Co_{0.7}CrFeNi_{1.7}$ HEA procured from TOSOH and SMD were used for both DED and SLM processing. The details of the processing conditions employed are mentioned in our previous studies.[36,37]

The as-deposited (AD) specimens from DED [referred to as DED(AD)] and SLM [referred to as SLM(AD)] were sectioned using the KENT USA (WSI-200) electric discharge machine (EDM). Sections from DED(AD) and SLM(AD) conditions were then individually encapsulated in a quartz tube backfilled with argon for the heat treatments (800°C for 5 h followed by water quenching). These conditions will be hereafter referred to as DED(HT) and SLM(HT).

Scanning electron microscopy (SEM) imaging was performed on all four conditions in an FEI-Quanta Nova-Nano SEM 230. Nanoindentation tests (Hysitron Inc., Minneapolis, MN, USA) were performed at room temperature (RT), 250°C and 500°C, using a Sapphire Berkovich tip. The tests were carried out at 1000 mN load with a loading time of 5 s, holding time of 2 s, and unloading time of 5 s; 50 μm spacing between indents was used to avoid overlap of plastic zones from adjacent indents. The high-temperature indentations were done in Ar + H_2 atmosphere to minimize oxidation of the samples, and the system was allowed to stabilize at each temperature for at least 15 min before performing the indentations. A minimum of 25 good indents were used for hardness calculations for statistics.

The phase fraction versus temperature plot for $Al_{0.3}Ti_{0.2}Co_{0.7}CrFeNi_{1.7}$ HEA was simulated using Thermo-Calc software (with TCHEA3 database).

RESULTS AND DISCUSSION

The SEM backscattered images from the as-deposited [DED(AD)] and the one-step annealed conditions [DED(HT)] of the DED processed $Al_{0.3}Ti_{0.2}Co_{0.7}CrFeNi_{1.7}$ HEA are shown in Fig. 1a–c and d–e, respectively. The DED as-deposited condition shows a single-phase (FCC) microstructure with reasonably large peculiar-shaped[38] grains often with jagged grain boundaries. Additionally, some grains also exhibit solidification cells presumably arising from compositional segregation because of the high solidification rates involved in DED processing. However, the possible formation of early-stage nanoscale $L1_2$ precipitates within the FCC matrix of the DED(AD) condition was previously observed in high-energy synchrotron x-ray diffraction results.[36] The annealing heat
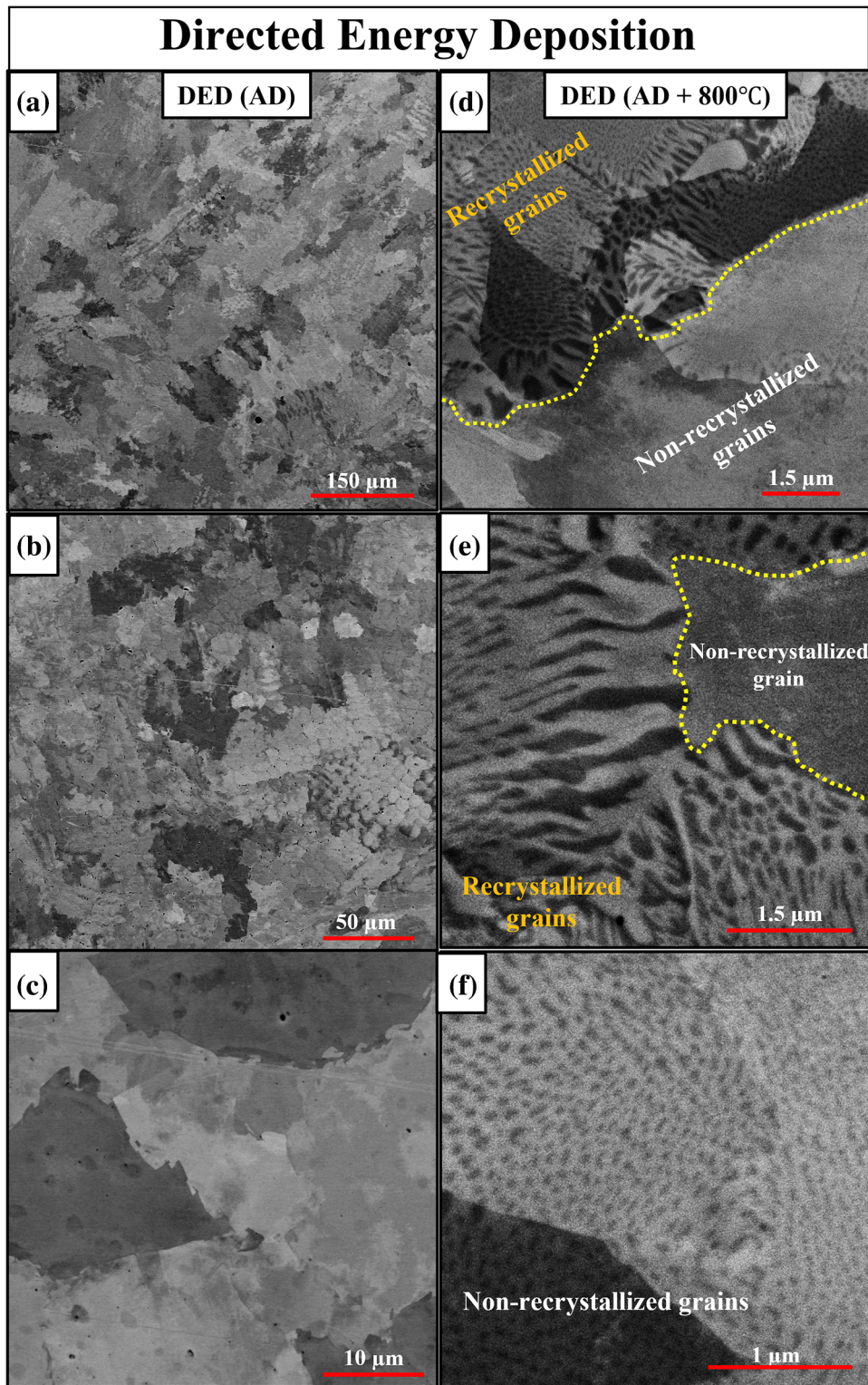
Fig. 1. Low, Medium, and High magnification SEM backscattered images for (a–c) DED (AD) and (d–f) DED (HT or AD + 800°C) conditions of DED processed $Al_{0.3}Ti_{0.2}Co_{0.7}CrFeNi_{1.7}$ HEA.

treatment (800°C for 5 h) conducted on the DED-processed HEA led to the partial recrystallization of FCC grains and a significant growth of the non-recrystallized FCC grains. The grain size of the non-recrystallized grains increased from ~ 81 μm in the DED(AD) to ~ 159 μm in the DED(HT) condition.[36]

Microstructure and Temperature Dependent Indentation Response of Additively Manufactured Precipitation-Strengthened Al$_{0.3}$Ti$_{0.2}$Co$_{0.7}$CrFeNi$_{1.7}$ High Entropy Alloy

5049

The annealing heat treatment also resulted in the formation of L1$_2$ precipitates with two different morphologies within the FCC matrix. The SEM images in Fig. 1d, e reveal the rod-like L1$_2$ precipitates in the recrystallized FCC grains, while the SEM image in Fig. 1f shows the equiaxed/near-spherical L1$_2$ precipitates in the non-recrystallized grains. The precipitation mechanism fundamentally differs between the two kinds of grains: continuous precipitation in the non-recrystallized grains and discontinuous precipitation in the recrystallized grains, leading to different morphologies for the L1$_2$ precipitates.[36]

The SEM backscattered images from the as-deposited [SLM(AD)] and the one-step annealed conditions [SLM(HT)] of the SLM processed Al$_{0.3}$Ti$_{0.2}$Co$_{0.7}$CrFeNi$_{1.7}$ HEA are shown in Fig. 2a–c) and d–e, respectively. The SLM(AD) condition exhibits elongated FCC grains, possibly growing epitaxially, with a significant fraction of solidification cells involving substantial compositional segregation (Fig. 2a, b). Unlike the DED(AD) condition, the intercellular walls in the SLM(AD) condition exhibited a BCC + B2 microstructure.[37] The high-magnification SEM image of the intercellular region in Fig. 2c clearly shows the fine-scale B2 precipitates in the darker BCC phase inside the cell wall. The SLM(AD) condition also showed early-stage nanoscale L1$_2$ precipitates within the FCC matrix.[37] The microstructures of the one-step annealed condition, SLM(HT), presented in Fig. 2d–f appears to be identical to the DED(HT) condition (Fig. 1d–f). However, the L1$_2$ precipitates in the SLM(HT) condition are marginally more refined than in the DED(HT) condition. The grain sizes in the as-deposited ($\sim$50 μm) and one-step annealed conditions ($\sim$20 μm) are also lower in the case of the SLM-processed alloy compared to the DED-processed counterpart.

In short, the as-deposited conditions of DED and SLM-processed HEA exhibited predominantly single-phase FCC microstructure with a negligible fraction of L1$_2$ precipitates. Although the SLM(AD) condition revealed B2 + BCC microstructure in the intercellular regions between solidification cells, it is shown to have an insignificant effect on the mechanical properties owing to its low phase fraction as well as large separation distances.[37] On the other hand, both heat-treated conditions, SLM(HT) and DED(HT), exhibited hierarchically heterogeneous microstructures at multiple length scales; finer recrystallized *FCC grains with* rod-like L1$_2$ precipitates and coarser non-recrystallized FCC grains with equiaxed/spherical L1$_2$ precipitates.

The nanoindentation tests were performed at three different temperatures, RT, 250°C, and 500°C for all four AM processed HEA conditions. The resultant hardness versus temperature plots are presented in Fig. 3, and the corresponding hardness values are listed in Table I. The % loss (reduction) in hardness between the two

temperatures, RT and 500°C, is calculated for all four conditions using the equation: % loss (reduction) = $\frac{Hardness(RT) - Hardness(500°C)}{Hardness(RT)}$, and the calculated values are listed in the last column of Table I. The heat-treated conditions [DED(HT) and SLM(HT)] exhibited remarkably higher hardness values ($>$ 4.3 GPa) at all three temperatures compared to the as-deposited conditions of this AM-processed HEA. This increase in the hardness can be attributed to the significantly higher phase fraction of the L1$_2$ precipitates in the heat-treated conditions as opposed to the much lower fractions of precipitates observed in the as-deposited conditions. The anticipated decrease in the hardness with an increase in the temperature from RT to 500°C is observed for all four conditions (Fig. 3). However, the % reduction in the hardness values for the as-deposited conditions [23.1% for DED(AD) and 13.3% for the SLM(AD)] is substantially higher than the heat-treated conditions [6.5% for DED(HT) and 4.9% for SLM(HT)]. This large difference in the % reduction in the hardness values can be attributed mainly to two factors: (1) relieving of stored residual stresses in the as-deposited conditions during the high-temperature testing and (2) to the softer single-phase FCC microstructure compared to the harder hierarchical multi-phase microstructures in the heat-treated conditions. It should be emphasized that the lower values of % reduction in hardness with an increase in temperature in the heat-treated conditions further signify the stability of the hierarchically heterogeneous microstructures at elevated temperatures.

While both DED and SLM as-deposited conditions showed nearly identical hardness values at RT, the SLM(AD) condition showed significantly higher hardness than the DED(AD) condition at elevated temperatures, especially at 500°C (Fig. 3c). However, the heat-treated conditions, DED(HT) and SLM(HT), showed practically overlapping performance at all three temperatures, as shown in Fig. 3d. The load versus displacement (P-h) curves obtained from the nanoindentation tests for all four conditions are presented in Fig. 4. Serrated yielding behavior, also known as Portevin-Le Chatlier (PLC) effect, was observed in the loading portion of the (P-h) curves for the DED(AD) and SLM(AD) conditions tested at 500°C as shown in Fig. 4c. These perturbations or discontinuities indicate the mechanical instability of the microstructure during the deformation process. The serrated yielding behavior in metals or alloys is commonly associated with the activation of a heterogenous dislocation source and its multiplication under loading.[39] However, Schuh's[40] review on "*Nanoindentation studies of materials*" additionally points out that phase transformations that occur during the nanoindentation process could also result in the serrated yielding or the PLC effect.[41] Therefore, microstructural characterization was performed on DED(AD) and
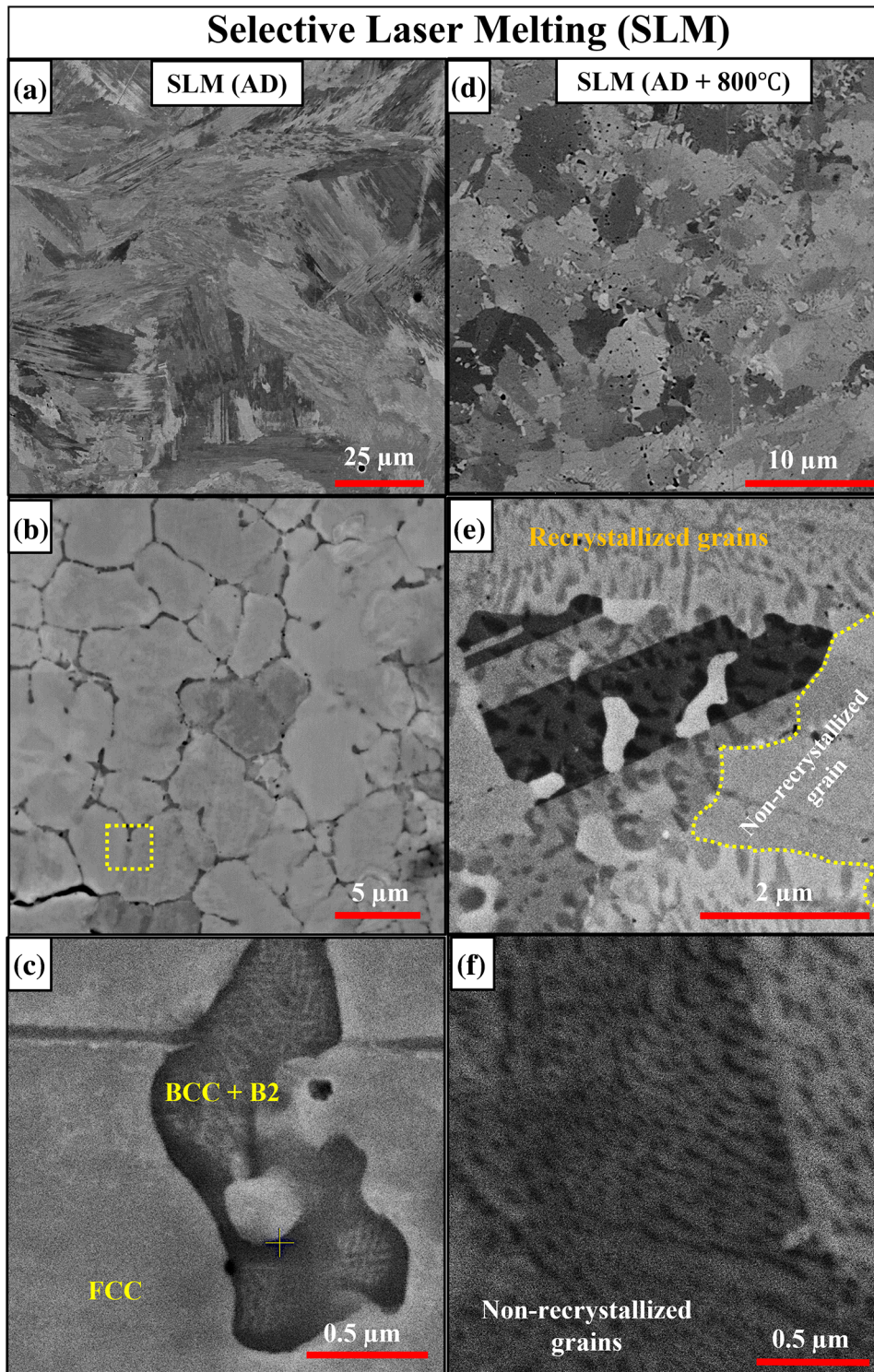
Fig. 2. Low, medium, and high-magnification SEM backscattered images for (a-c) SLM (AD) and (d-f) SLM (HT or AD + 800°C) conditions of SLM processed $Al_{0.3}Ti_{0.2}Co_{0.7}CrFeNi_{1.7}$ HEA.

SLM(AD) conditions post-nanoindentation (at 500°C), and the resultant SEM backscattered images are presented in Fig. 5a, b and c, d, respectively. Features resembling $L1_2$ precipitates

were present in both conditions demonstrating the possibility of dynamic precipitation of the $L1_2$ phase within the FCC matrix during the nanoindentation testing at 500°C. Moreover, the phase fraction
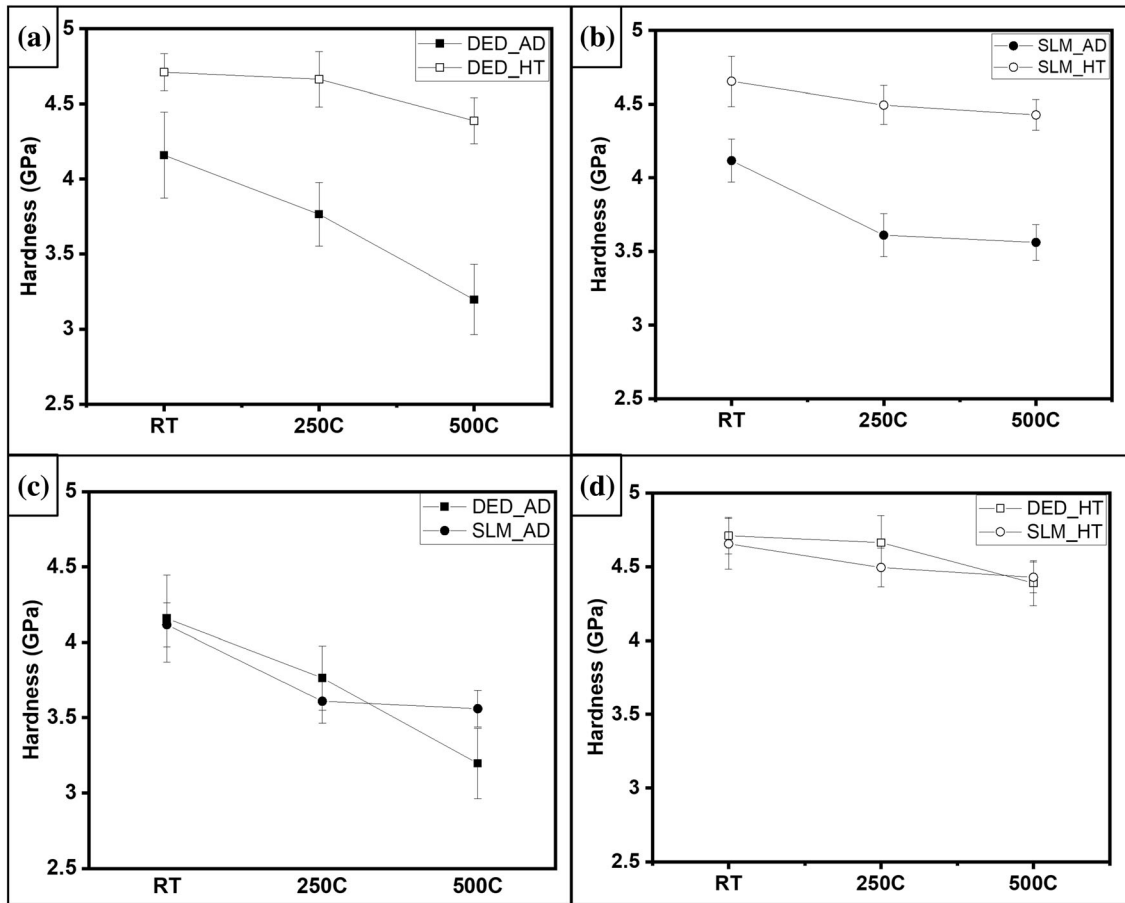
Fig. 3. Hardness versus temperature plots comparing (a) DED (AD) and DED (HT) conditions, (b) SLM(AD) and SLM (HT) conditions, (c) DED(AD) and SLM(AD) conditions, and (d) DED(HT) and SLM(HT) conditions of the AM processed $Al_{0.3}Ti_{0.2}Co_{0.7}CrFeNi_{1.7}$ HEA.

Table I. Nanoindentation hardness (in GPa) values for all four conditions of AM processed $Al_{0.3}Ti_{0.2}Co_{0.7}CrFeNi_{1.7}$ HEA

AM method	Condition	RT	250°C	500°C	% Loss
DED	AD	4.157 ± 0.287	3.763 ± 0.212	3.197 ± 0.233	23.13 ↓
	AD + 800°C (HT)	4.710 ± 0.123	4.663 ± 0.183	4.387 ± 0.153	6.5↓
SLM	AD	4.116 ± 0.145	3.569 ± 0.171	3.560 ± 0.121	13.3↓
	AD + 800°C (HT)	4.654 ± 0.171	4.494 ± 0.132	4.427 ± 0.104	4.9↓

versus temperature prediction for this HEA ($Al_{0.3}Ti_{0.2}Co_{0.7}CrFeNi_{1.7}$) presented in Fig. 6 revealed almost 40% for the $L1_2$ phase at 500°C. It is envisaged that dynamic precipitation pins down the mobile dislocations, restoring the hardness locally during the deformation.[42,43] Therefore, the serrated yielding observed in the DED(AD) and SLM(AD) conditions during the nanoindentation loading (at 500°C) could be mainly due to the precipitation of the $L1_2$ phase within the FCC matrix.

Notably, the same serrated behavior is not observed for SLM(AD) or DED(AD) conditions tested at RT or 250°C (Fig. 4c). The SEM investigation also did not reveal any obvious precipitation of the L12 phase in an independent study previously conducted by the authors. The phase fraction versus temperature plot (in Fig. 6) exhibits no significant change in the $L1_2$ phase fraction for temperatures < 500°C. Therefore, it is intuitive that sluggish diffusion at lower temperatures makes the $L1_2$ precipitation kinetically unfavorable. Hence, no
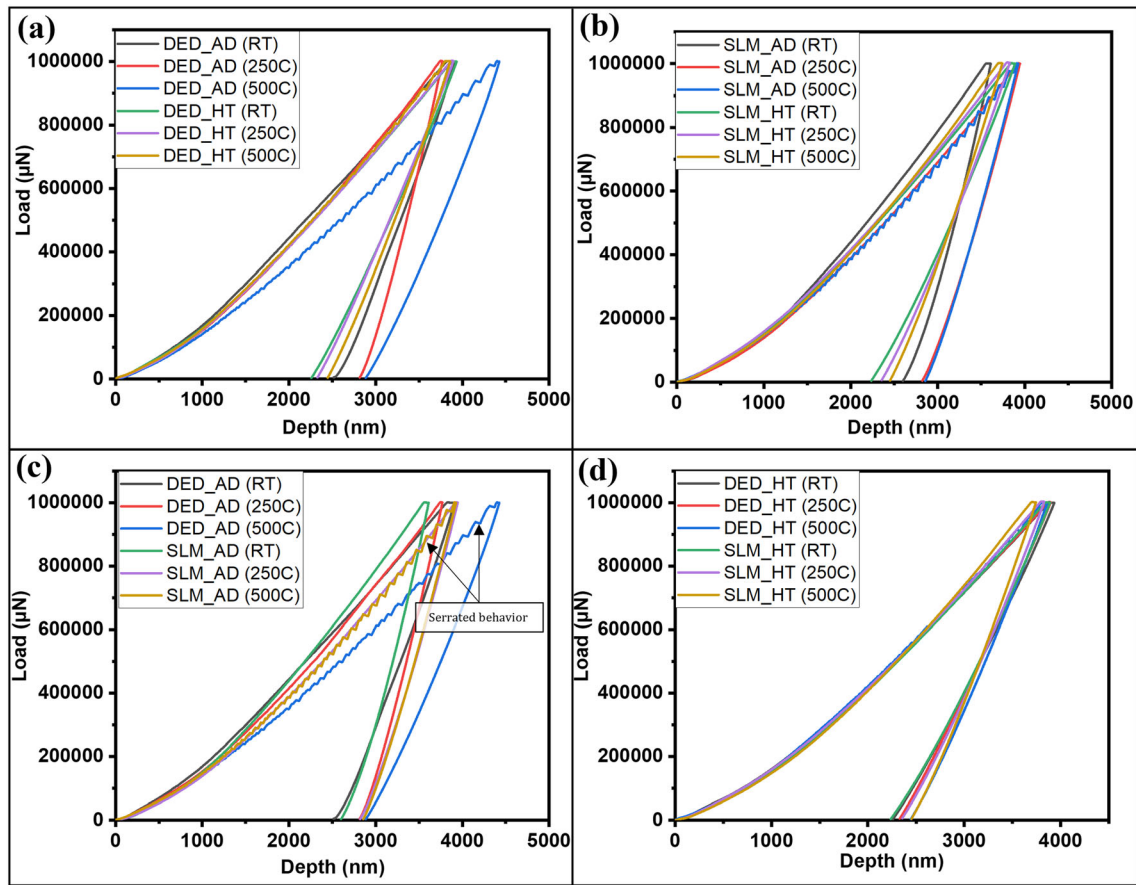
Fig. 4. Representative load versus displacement (P-h) curves as a function of temperature comparing (a) DED (AD) and DED (HT) conditions, (b) SLM (AD), and SLM(HT) conditions, (c) DED(AD) and SLM(AD) conditions, and (d) DED(HT)and SLM(HT) conditions of AM processed $Al_{0.3}Ti_{0.2}Co_{0.7}CrFeNi_{1.7}$ HEA.

serrations were observed in the P-h curves for DED(AD) and SLM(AD) conditions tested at RT and 250°C. Similarly, the P-h curves in Fig. 4d for DED(HT) and SLM(HT) conditions did not reveal any signs of serrated yielding during nanoindentation, which again illustrates the stability of the hierarchically heterogeneous microstructures during deformation at elevated temperatures.

CONCLUSION

In summary, the temperature-dependent (from RT to 500°C) nanoindentation behavior of the DED and SLM processed $Al_{0.3}Ti_{0.2}Co_{0.7}CrFeNi_{1.7}$ HEA was investigated in the as-deposited and one-step annealed conditions for this study. The hierarchically heterogeneous microstructures obtained via simple one-step annealing of the DED and SLM-processed HEA exhibited significantly better performance than the nearly homogeneous microstructures in the as-deposited state. The one-step annealed conditions revealed $< 6.6\%$ reduction in hardness values at 500°C compared to RT, while the as-deposited conditions showed $> 18\%$ reduction in hardness between RT and 500°C. The one-step

annealed conditions also exhibited significantly higher hardness than the as-deposited conditions owing to their multi-phase (FCC + $L1_2$) microstructures with a substantial fraction of ordered $L1_2$ precipitates. Furthermore, serrated yielding (PLC effect) indicative of microstructural instability was observed during nanoindentation deformation (at 500°C) for both SLM and DED processed conditions but not after the one-step annealing. Overall, the nanoindentation results signify the stability of these hierarchically heterogeneous microstructures developed via single-step annealing, exploiting the residual stresses, in the AM processed $Al_{0.3}Ti_{0.2}Co_{0.7}CrFeNi_{1.7}$ HEA. The results presented in this study open up strong possibilities for applications of HEAs in high-temperature nuclear reactors.

RECOMMENDATIONS

Future work may include investigating this material's behavior for a variety of environment, molten salt corrosion behavior and air oxidation behavior at temperatures > 800°C. The obtained results can be compared with other high-temperature application materials such as the ODS (PM 2000) and AFA alloys.
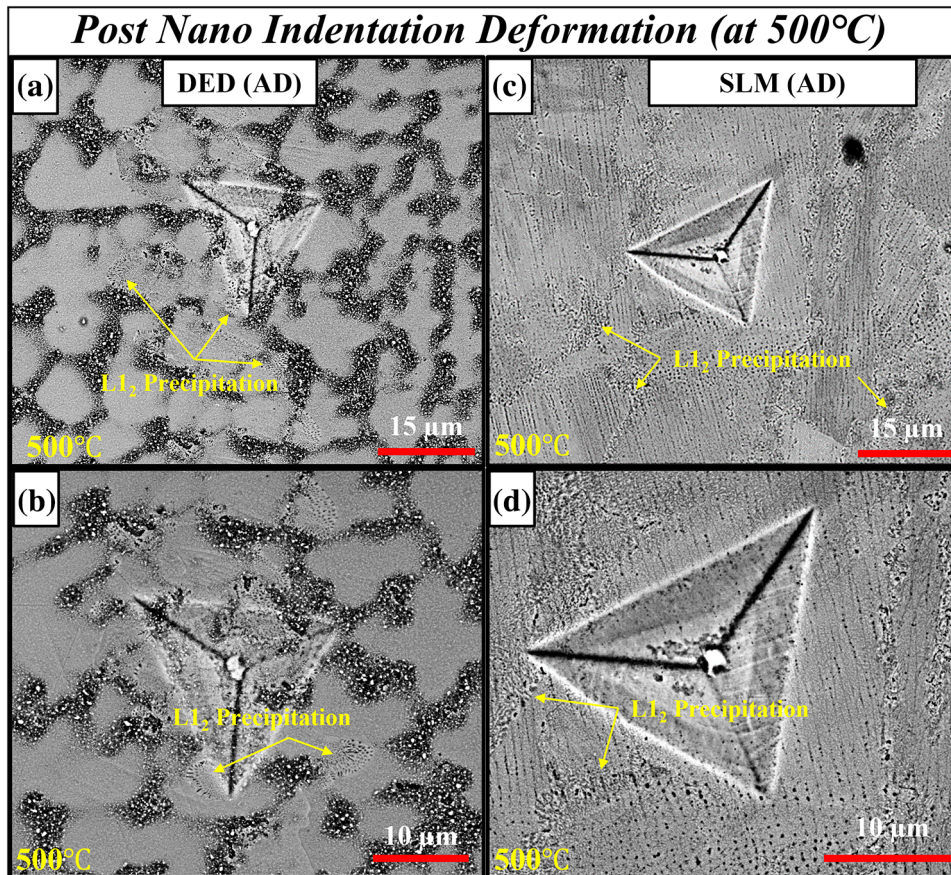
Fig. 5. SEM backscattered Images revealing the L1$_2$ precipitation post nano-indentation deformation at 500°C for (a, b) DED (AD) and (c, d) SLM(AD) conditions of the AM processed HEA.
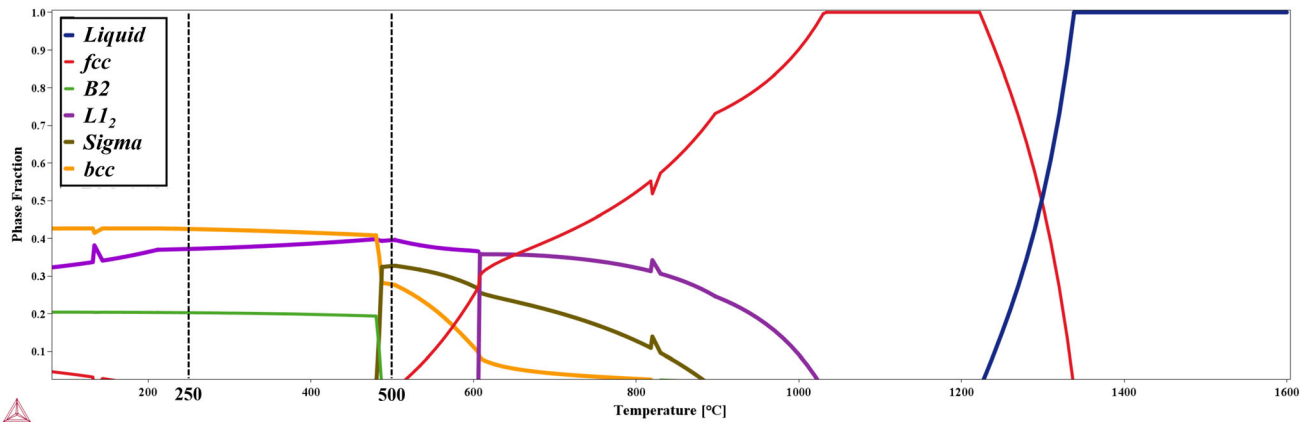

Fig. 6. Phase fraction vs temperature plot for Al$_{0.3}$Ti$_{0.2}$Co$_{0.7}$CrFeNi$_{1.7}$ high-entropy alloy (HEA) generated using Thermo-Calc software.

CONFLICT OF INTEREST

On behalf of all authors, the corresponding author states that there is no conflict of interest.

REFERENCES

1. M. Sadeghilaridjani, A. Ayyagari, S. Muskeri, V. Hasannaeimi, J. Jiang, and S. Mukherjee, *JOM* 72, 123 (2020).
2. J. Brechtl, S. Agarwal, M.L. Crespillo, J. Salasin, T. Yang, H. Bei, and S.J. Zinkle, *Intermetallics (Barking)* 116, 106655 (2020).
3. A.G. Perez-Bergquist, H. Bei, K.J. Leonard, Y. Zhang, and S.J. Zinkle, *Intermetallics (Barking)* 53, 62 (2014).
4. B. Wang, X. Mei, H. Zhang, W. Hou, Y. Wang, Z. Wang, and C. Dong, *J. Nucl. Mater.* 444(1), 342 (2014).
5. R. Schäublin, A. Ramar, N. Baluc, V. de Castro, M.A. Monge, T. Leguey, N. Schmid, and C. Bonjour, *J. Nucl. Mater.* 351, 247 (2006).
6. Z.F. Wu, L.D. Xu, H.Q. Chen, Y.X. Liang, J.L. Du, Y.F. Wang, S.L. Zhang, X.C. Cai, B.R. Sun, J. Zhang, T.D. Shen, J. Wang, and E.G. Fu, *J. Nucl. Mater.* 559, 153418 (2022).
7. G.R. Odette, M.J. Alinger, and B.D. Wirth, *Annu. Rev. Mater. Res.* 38, 471 (2008).
8. A. Kozlovskiy, I. Kenzhina, Z.A. Alyamova, and M. Zdorovets, *Opt. Mater.* 91, 130 (2019).
9. M. Khafizov, J. Pakarinen, L. He, and D.H. Hurley, *J. Am. Ceram. Soc.* 102, 7533 (2019).
10. K. Liu, K. Zhang, T. Deng, B. Luo, and H. Zhang, *J. Nucl. Mater.* 538, 152236 (2020).
11. F. Wang, X. Yan, T. Wang, Y. Wu, L. Shao, M. Nastasi, and B. Cui, *Acta Mater.* 195, 739 (2020).
12. J.-W. Zhang, I.J. Beyerlein, and W.-Z. Han, *Phys. Rev. Lett.* 122(25), 255501 (2019).
13. H. Deng, Z.-J. Li, L. Wang, L.-Y. Yuan, J.-H. Lan, Z.-Y. Chang, Z.F. Chai, and W.Q. Shi, *ACS Appl. Nano Mater.* 2(4), 2283 (2019).
14. L.F. Zhang, R. Gao, J. Hou, B.L. Zhao, M. Sun, and T. Hao, *J. Nucl. Mater.* 543, 152548 (2021).
15. Y. Liu, Y. Zeng, Q. Guo, J. Zhang, Z. Li, D.-B. Xiong, X. Li, and D. Zhang, *Acta Mater.* 196, 17 (2020).
16. W. Han, M.J. Demkowicz, N.A. Mara, E. Fu, S. Sinha, A.D. Rollett, Y. Wang, J.S. Carpenter, I.J. Beyerlein, and A. Misra, *Adv. Mater.* 25, 6975 (2013).
17. E.J. Pickering, A.W. Carruthers, P.J. Barron, S.C. Middleburgh, D.E.J. Armstrong, and A.S. Gandy, *Entropy* 2021(23), 98 (2021).
18. S.J. Zinkle, and L.L. Snead, *Annu. Rev. Mater. Res.* 44, 241 (2014).
19. O. El-Atwani, N. Li, M. Li, A. Devaraj, J.K.S. Baldwin, M.M. Schneider, D. Sobieraj, J.S. Wróbel, D. Nguyen-Manh, S.A. Maloy, and E. Martinez, *Sci. Adv.* https://doi.org/10.1126/sciadv.aav2002 (2019).
20. A.S. Gandy, B. Jim, G. Coe, D. Patel, L. Hardwick, S. Akhmadaliev, N. Reeves-McLaren, and R. Goodall, *Front. Mater.* https://doi.org/10.3389/fmats.2019.00146 (2019).
21. A. Ayyagari, R. Salloom, S. Muskeri, and S. Mukherjee, *Materialia* 4, 99 (2018).
22. O.A. Waseem, and H.J. Ryu, *Sci. Rep.* https://doi.org/10.1038/s41598-017-02168-3 (2017).

23. T. Nagase, S. Anada, P.D. Rack, J.H. Noh, H. Yasuda, H. Mori, and T. Egami, *Intermetallics* 26, 122 (2012).
24. T. Nagase, S. Anada, P.D. Rack, J.H. Noh, H. Yasuda, H. Mori, and T. Egami, *Intermetallics* 38, 70 (2013).
25. S.Q. Xia, X. Yang, T.F. Yang, S. Liu, and Y. Zhang, *JOM* 67, 2340 (2015).
26. T. Nagase, P. Rack, J. Noh, and T. Egami, *Intermetallics* 59, 32 (2015).
27. S. Xia, Z. Wang, T. Yang, and Y. Zhang, *J. Iron Steel Res. Int.* 22(10), 879 https://doi.org/10.1016/S1006-706X(15)30084-4 (2015).
28. S.C. Middleburgh, D.M. King, and G.R. Lumpkin, *R. Soc. Open sci.* 2(6), 140292 https://doi.org/10.1098/RSOS.150193 (2015).
29. D.J.M. King, P.A. Burr, E.G. Obbard, and S.C. Middleburgh, *J. Nucl. Mater.* 488, 70 (2017).
30. P. Agrawal, S. Gupta, A. Dhal, R. Prabhakaran, L. Shao, and R.S. Mishra, *J. Nucl. Mater.* 574, 154217 (2023).
31. A. Kareer, J.C. Waite, B. Li, A. Couet, D.E.J. Armstrong, and A.J. Wilkinson, *J. Nucl. Mater.* 526, 151744 (2019).
32. B. Kombaiah, Y. Zhou, K. Jin, A. Manzoor, J.D. Poplawsky, J.A. Aguiar, H. Bei, D.S. Aidhy, P.D. Edmondson, and Y. Zhang, *ACS Appl. Mater. Interfaces* 15, 3912 (2023).
33. B. Gwalani, S. Dasari, A. Sharma, V. Soni, S. Shukla, A. Jagetia, P. Agrawal, R.S. Mishra, and R. Banerjee, *Acta Mater.* 219, 117234 (2021).
34. Y. Zhao, Z. Chen, K. Yan, S. Naseem, W. Le, H. Zhang, and W. Lu, *Mater. Sci. Eng. A* 838, 142759 (2022).
35. S. Dasari, A. Jagetia, Y.J. Chang, V. Soni, B. Gwalani, S. Gorsse, A.C. Yeh, and R. Banerjee, *J. Alloys Compd.* 830, 154707 (2020).
36. M.S.K.K.Y. Nartu, A. Chesetti, S. Dasari, A. Sharma, S.A. Mantri, N.B. Dahotre, and R. Banerjee, *Mater. Sci. Eng. A* 849, 143505 (2022).
37. A. Chesetti, S. Banerjee, S. Dasari, S.M. Varahabhatla, A. Sharma, S.A. Mantri, M.S.K.K.Y. Nartu, N. Dahotre, and R. Banerjee, *Addit. Manuf. Lett.* 6, 100140 (2023).
38. M.S.K.K.Y. Nartu, A. Jagetia, V. Chaudhary, S.A. Mantri, E. Ivanov, N.B. Dahotre, R.V. Ramanujan, and R. Banerjee, *Scr. Mater.* 187, 30 (2020).
39. V. Kumar, A. Gupta, D. Lahiri, and K. Balani, *J. Phys. D Appl. Phys.* 46, 145304 (2013).
40. C.A. Schuh, *Mater. Today* 9, 32 (2006).
41. J. Il Jang, M.J. Lance, S. Wen, T.Y. Tsui, and G.M. Pharr, *Acta Mater.* 53, 1759 (2005).
42. S. Banerjee, and U.M. Naik, *Acta Mate.* 44, 3667 (1996).
43. D. Choudhuri, S.A. Mantri, T. Alam, S. Banerjee, and R. Banerjee, *Scr. Mater.* 124, 15 (2016).